

Effect of heat treatment on microstructural evolution and mechanical properties of eutectic Al-6Mg₂Si alloy processed by laser powder bed fusion

Tao Wen^a, Jianying Wang^a, Feipeng Yang^a, Mengzhen Zhu^a, Yimou Luo^a, Zhilin Liu^b, Xixi Dong^c, Hailin Yang^{a*}, Shouxun Ji^d

a. State Key Laboratory of Powder Metallurgy Central South University, Changsha 410083, China

b. Light Alloy Research Institute, College of Mechanical and Electrical Engineering, Central South University, Changsha, 410083, P.R. China

c. College of Mechanical and Electrical Engineering, Nanjing University of Aeronautics and Astronautics, Nanjing, 210016, China

d. Brunel Centre for Advanced Solidification Technology (BCAST), Brunel University London, Uxbridge, Middlesex UB8 3PH, United Kingdom

* Corresponding authors: y-hailin@csu.edu.cn

Abstract: It is critical to tailor specific schemes of heat treatment for alloys manufactured by laser powder bed fusion according to their typical microstructural characteristics. This study systematically investigated the influence of direct ageing, annealing treatment, and solution ageing treatment on the microstructural evolution and mechanical properties of the L-PBFed Al-6Mg₂Si alloy. The results demonstrated that the hierarchical microstructure of L-PBFed Al-6Mg₂Si alloy mainly consists of fine α -Al grains, Al/Mg₂Si cellular structures, solutes, and high-density dislocations, providing yield strength of 363 MPa, ultimate tensile strength of 436 MPa, and elongation of 9.3%. Under DA condition, the Al/Mg₂Si cellular structure was preserved while promoting the precipitation of fine β'' precipitates. The DA sample exhibited significant improvements in mechanical properties, with YS, UTS, and El of 420 MPa, 496 MPa, and 9.5%, respectively. In contrast, the eutectic Al/Mg₂Si cellular structure was totally destroyed and subsequently transformed to coarse Mg₂Si particles under AT and SAT conditions, resulting in strength degradation. Therefore, direct ageing is a suitable heat treatment process to acquire a good strength-ductility synergy of the L-PBFed Al-Mg₂Si alloy in this work.

Keywords: Al-Mg₂Si alloys; Laser powder bed fusion; Heat treatment; Microstructures; Mechanical properties.

1. Introduction

Laser powder bed fusion (L-PBF) has attracted widespread research attention for production of customized metallic complex parts that are impossible to manufacture via traditional methods (e.g. casting, forging, welding) [1, 2]. The L-PBF technology is characterised by high cooling rates (10^2 - 10^6 K/s) and high temperature gradient ($> 10^5$ °C/m), imparting the specific non-equilibrium microstructure and excellent mechanical properties [3, 4]. Recently, the L-PBFed aluminium alloy has received extensive interest due to the need for lightweight in the aerospace industry [5]. The commercial age-hardenable high-strength Al-Cu, Al-Mg-Si and Al-Zn-Mg-Cu alloys exhibit poor processability and hot cracking during printing process owing to their large solidification interval and the coarse columnar grains [6-8]. The most popular L-PBFed Al alloys are primarily the eutectic cast Al-Si alloys (e.g. AlSi12, AlSi10Mg, AlSi7Mg) [9, 10] and Scalmalloy® (Al-Mg-Sc-Zr) alloys [11, 12]. The former take advantage of the excellent fluidity of the typical eutectic network to mitigate stress, while the latter employs $Al_3(Sc, Zr)$ particles to encourage columnar-to-equiaxed transition, thereby enhancing resistance to hot cracking [13, 14]. Correspondingly, the other commercial Al alloys have been designed following the strategy of realizing grain refinement and eutectic filling to improve the L-PBF processability [15, 16].

Previous studies have shown that tailoring heat treatments provides an effective approach to acquire the comprehensive mechanical properties for L-PBFed Al alloys. The heat treatments of L-PBFed Al alloy can be classified into three types: (i) conventional T6 heat treatment (solution treatment followed by ageing); (ii) annealing treatment; and (iii) direct ageing treatment. For Al-Si based alloys, the T6 heat treatment normally disrupts the unique cellular structure and significantly coarsens the eutectic Si, resulting in the reduction of strength but the improvement in ductility. For instance, the L-PBFed AlSi10Mg alloy decreases the YS/UTS from 304/486 MPa to 181/281 MPa, while the El increases from 11.9 % to 14.8 % under T6 heat treatment [17]. Meanwhile, the effect of T6 treatment has been extended to the printable modified Al-Cu-Mg and Al-Zn-Mg based alloys. It has been investigated that the UTS increased from 365 MPa to 432 MPa, but the El decreased from 12 % to 10 % in the L-PBFed Al-Cu-Mg-Ti alloy under T6 heat treatment [6]. Similarly, the Al-Zn-Mg-Sc-Zr alloy shows outstanding mechanical response under T6 heat treatment, providing a UTS of 435 MPa and El of 11.1 % [18].

It is worth noting that the annealing treatment is a common strategy to reduce residual stresses from thermal cycling of L-PBFed Al alloys. A treatment of annealing

at 300 °C for a period of 1-2 h is normally applied to release the stress and enhance the ductility of L-PBFed AlSi10Mg alloy with the corresponding reduction in strength [19, 20]. Meanwhile, the strength shows a gradual diminish when treating with increased annealing temperatures because of the disruption of eutectic Si cellular structure and the enrichment of Si particles [21, 22]. In contrast, the direct ageing holds a huge potential in preserving a typical hierarchical structure of L-PBFed alloys. The direct ageing treatment at comparatively low temperatures (120 – 200 °C) can enhance strength through precipitation hardening of nanoscale Mg-Si and Si precipitates in L-PBFed Al-Si based alloys. For example, the L-PBFed AlSi10Mg alloy exhibits YS of ~ 310 MPa and El of 6.2 % after direct aging at 180 °C/ 6h [23]. The promotion of nanoscales Al₃(Sc, Zr) particles in L-PBFed Al-Mg-(Si)-Sc-Zr alloy also enhance the yield strength after direct ageing at 300 °C [12, 24]. Clearly, it is critical to tailor specific schemes of heat treatment in the L-PBFed Al alloy according to their typical microstructural characteristics, and a correlation between the heat treatment process, microstructural evolution and mechanical response of L-PBFed Al alloys need to be investigated systematically.

The Al-Mg-Si ternary system can be denoted as Al-Mg₂Si pseudo-binary eutectic system when the Mg/Si weight ratio becomes 1.73, which exerts a strong ability for crack elimination and strength enhancement [25-27]. In our pervious study [28], the effects of Mg₂Si content on the processability and mechanical response of L-PBFed Al-Mg₂Si alloy (3-12 wt. % Mg₂Si) were investigated. However, the microstructural evolution and mechanical response of the L-PBFed Al-Mg₂Si alloy to heat treatment remain unclear. This also brings out some interesting issues: (i) the correlation between heat treatment and microstructural features of the L-PBFed Al-Mg₂Si alloy, including typical melt pool structures and eutectic Al/Mg₂Si cellular structure; (ii) the effectiveness of heat treatment in improving mechanical properties, and the corresponding strengthening mechanisms; (iii) determining the optimum heat treatment scheme for L-PBFed Al-Mg₂Si alloy to achieve excellent strength-ductility synergy. Therefore, this work mainly aims to revealing the microstructural evolution and mechanical response of L-PBFed Al-Mg₂Si alloy during following treatments of direct ageing, annealing and solid solution with sequent ageing treatment. The discussion focuses on the microstructural characteristics, especially variation in cellular structure and the nanoscale precipitates formed after the different heat treatments, as well as the strengthening mechanisms.

2. Experimental methods

2.1 Powder and sample preparation

Al-6Mg₂Si pre-alloyed powders were fabricated via gas atomization. The mean size of Al-6Mg₂Si pre-alloyed powders with spherical or near spherical shapes is 27.1 μm . The chemical compositions of the Al-6Mg₂Si powders were evaluated with inductively coupled plasma atomic emission spectrometry (ICP-AES) in **Table 1**. Al-6Mg₂Si alloy was manufactured using L-PBF machine (EP-M150) from E-Plus-3D Co.,Ltd. Correspondingly, the optimized printing parameters for obtaining highest relative density were as follows: laser powder (P) was 310 W, scan speed (v) was 1000 mm/s, layer thickness (t) was 0.03 mm, hatch spacing (h) was 0.1 mm, and laser energy density ($VED=P/vht$) was 103.3 J/mm³. The printed cubic samples and cuboid samples were $10 \times 10 \times 10 \text{ mm}^3$ and $80 \times 10 \times 10 \text{ mm}^3$ in size for subsequent microstructural characterization and mechanical testing, respectively.

Table 1. Chemical compositions of the Al-6Mg₂Si powders measured by ICP-AES (wt.%).

| Alloy | Mg | Si | Mn | Fe | Others | Al |
|------------------------|------|------|------|------|--------|------|
| Al-6Mg ₂ Si | 3.88 | 2.15 | 0.54 | 0.18 | <0.08 | Bal. |

2.2 Heat treatment and mechanical testing

The direct ageing treatment (DA) was performed at 150 °C, 180 °C and 210 °C for 1 – 24 h followed by air cooling. The annealing treatment (AT) was selected at 300 °C for 1- 10 h with subsequent air cooling. The solution + ageing treatment (SAT) was treated at a temperature of 490 °C for 1 h with water quenching, and subsequent 150 °C for 1 – 10 h followed by air cooling. The microhardness was measured using the Vickers microhardness tester with the 200 g load for the standing time of 15 s. The average microhardness was calculated from at a minimum 10 points for alloy sample. The cuboid sample was fabricated into the dog-bone-shaped tensile samples with a 15 mm in length, 4 mm in width and 2 mm in thickness using electrical discharge machining (EDM). Quasi-static tensile properties were carried out by testing machine, and the engineering strain rate was $1 \times 10^{-3} \text{ s}^{-1}$. The average of data was obtained from at least three measurements.

2.3 Microstructural characterization

The surface morphology and pores of samples were measured by optical microscope (OM). The phase analysis was performed by X-ray diffraction instrument (XRD) in the scanning range of 20°-80°. The typical solidification microstructure was characterized via scanning electron microscope (SEM). The Keller solution was used

to etch the sample for SEM observation. SEM was performed at an acceleration voltage of 10 kV and the working distance of 5 mm. The grain morphology and size were measured by electron backscattered diffraction (EBSD). EBSD measurements were carried out at an acceleration voltage of 30 kV with step size of 1.1 μm . Moreover, the microstructure evolution was performed by transmission electron microscope (TEM) further. The TEM samples were ground to 60 μm through silicon carbide sandpaper and thinned using precision ion polishing system (PIPS). TEM analysis was conducted at an acceleration voltage of 300 kV.

3. Results

3.1 Mechanical properties

Fig. 1 shows the Vickers microhardness and tensile strength curves of L-PBFed Al-6Mg₂Si alloy under different conditions. It is seen that the microhardness increases initially and then decreases with the prolonging ageing time at 150 °C and 180 °C, but the peak ageing time and microhardness were greatly different. The microhardness achieved the peaks at 150 °C for 8 h (DA-150) and 180 °C for 2 h (DA-180), corresponding to the values of 162.8 Hv and 154.9 Hv, respectively. It is also noted that the microhardness decreased significantly after ageing at 210 °C, and the value was 119.9 Hv at 210 °C for 4 h (DA-210). After annealing treatment and solution + ageing treatment, the microhardness of the samples decreases significantly. The microhardness reduced to 82.6 Hv and 74.6 Hv after annealing treatment at 300 °C for 4 h (AT-300) and solution + ageing treatment at 490 °C/1 h + 150 °C/8 h (SAT-490/150). Meanwhile, **Fig. 1b** illustrates the tensile strength curves of the samples, and the corresponding data are displayed in **Table 2**. The L-PBFed alloy exhibits the YS of 363 MPa, UTS of 436 MPa and El of 9.3 %, respectively. It is worth noting that the samples exhibited a superior strength-ductility synergy after DA-150 condition, in which the YS and UTS were significantly enhanced to 420 MPa and 496 MPa with an El of 9.5 %. After SAT-490/150 condition, the samples exhibited a striking decrease in strength with the YS of 130 MPa and UTS of 204 MPa.

Fig. 2 shows the fracture morphologies of L-PBFed Al-6Mg₂Si alloy under different conditions. In **Fig. 2(a&b)**, the fracture morphologies were mainly composed of tearing ridges and dimples for L-PBFed samples. The fracture modes of DA-150, DA-180, and DA-210 samples remained unchanged, exhibiting a distinct brittle-plastic mixed fracture mode, and the poor elongation in the DA-210 sample was primarily attributed to the presence of short and shallow dimples. In contrast, the AT-300 and SAT-490/150 samples displayed large and deep dimples, which was

indicative of typical ductile characteristics.

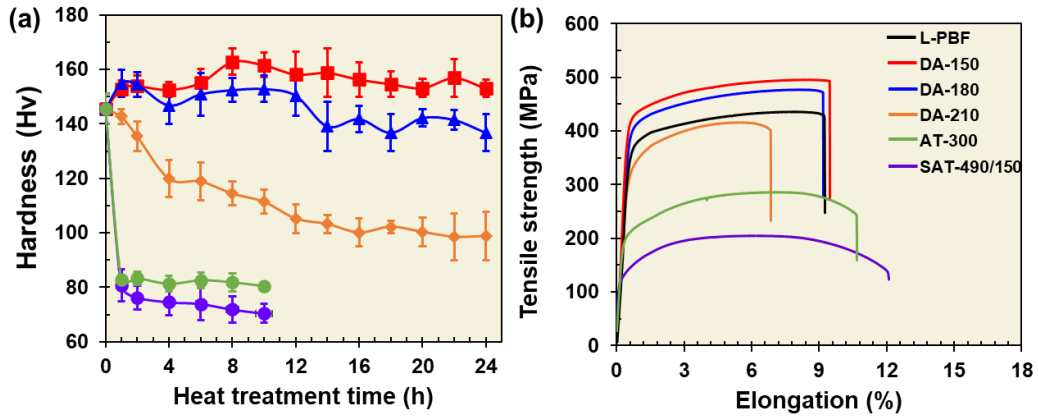


Fig. 1. (a) Microhardness curves and (b) tensile strength curves of the L-PBFed Al-6Mg₂Si alloy under different heat treatments.

Table 2 Mechanical properties of the L-PBFed Al-6Mg₂Si alloy under different conditions.

| Condition | Hardness (Hv) | YS (MPa) | UTS (MPa) | El (%) |
|-------------|---------------|----------|-----------|------------|
| L-PBF | 145.4 ± 5.9 | 363 ± 7 | 436 ± 12 | 9.3 ± 0.6 |
| DA-150 | 162.8 ± 3.6 | 420 ± 12 | 496 ± 20 | 9.5 ± 0.2 |
| DA-180 | 154.9 ± 2.2 | 404 ± 11 | 476 ± 20 | 9.2 ± 0.1 |
| DA-210 | 119.9 ± 3.5 | 338 ± 11 | 416 ± 14 | 6.9 ± 0.3 |
| AT-300 | 82.6 ± 1.2 | 205 ± 21 | 285 ± 11 | 10.7 ± 0.4 |
| SAT-490/150 | 74.6 ± 1.7 | 130 ± 3 | 204 ± 7 | 12.1 ± 0.9 |

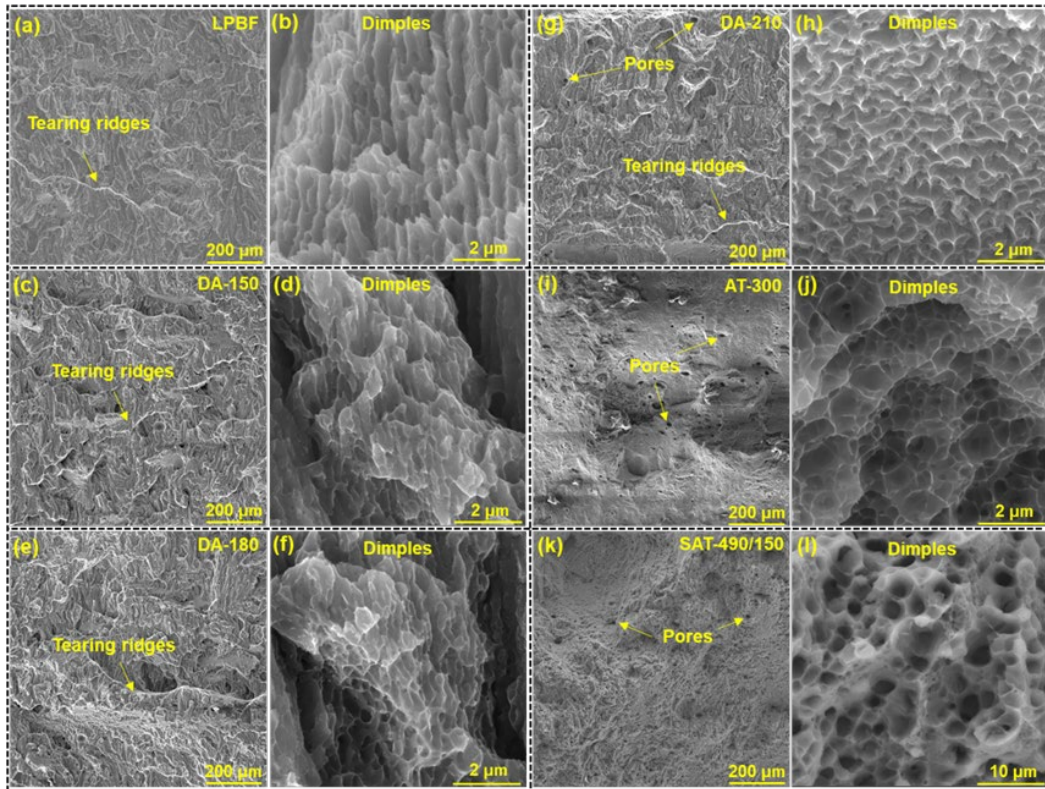


Fig. 2. SEM images showing the fractured morphology of Al-6Mg₂Si alloy: (a, b) L-PBFed; (c, d)

DA-150; (e, f) DA-180; (g, h) DA-210; (i, j) AT-300; (k, l) SAT-490/150.

3.2 Microstructural characterization

OM image of the Al-6Mg₂Si alloy under different conditions are illustrated in **Fig. 3**. In **Fig. 3a**, the Al-6Mg₂Si alloy exhibited an excellent printing processability with a high relative density (99.58 %). Meanwhile, the typical molten pool structure was clearly detected within the samples owing to the large temperature gradient and heat accumulation characteristics in L-PBF process. The samples still maintained the typical molten pool structure, with no significant variation in relative density and pores after the DA treatments (**Figs. 3b-d**). However, the molten pools were completely broken up and the pores increased significantly under the conditions of AT-300 and SAT-490/150, leading to a decrease in relative density (**Figs. 3e&f**). The XRD spectra of the Al-6Mg₂Si alloy are presented in **Fig. 4**. The phases presented in the L-PBFed samples were α -Al and Mg₂Si, with no significant phase variation observed after heat treatments. Furthermore, the Fe/Mn-enriched phases were not observed, which may be associated with the low volume fraction in all the samples. Furthermore, the peaks of the Mg₂Si phase were stronger in the samples under heart treatment conditions than that of in the L-PBFed samples, indicating the formation of more Mg₂Si phases.

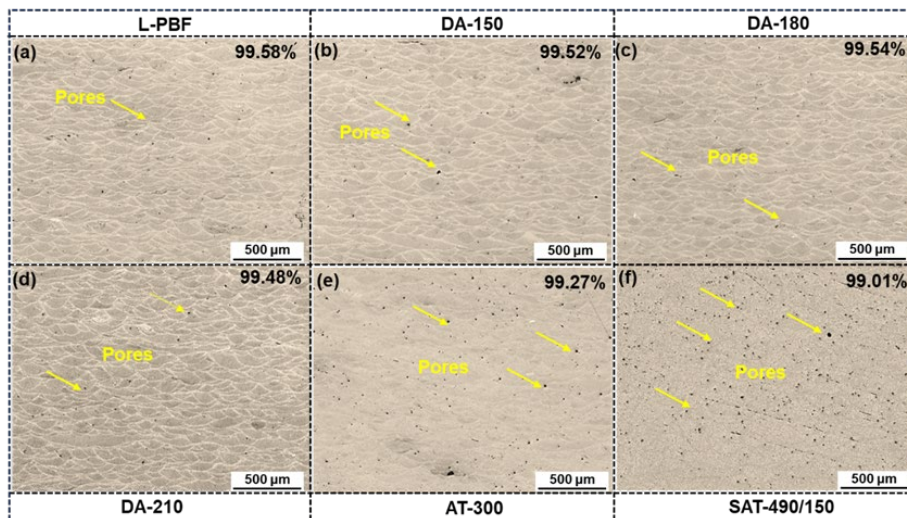


Fig. 3. OM image showing the molten pool structure and pores of the Al-6Mg₂Si alloy under different heat treatment conditions.

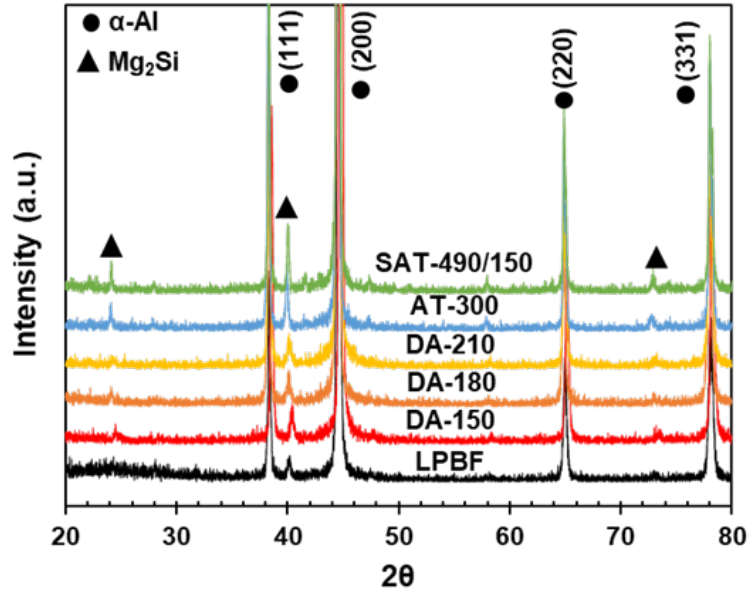


Fig. 4. XRD patterns of the Al-6Mg₂Si alloys under different conditions.

SEM analysis with EDS mapping were applied to analyse the microstructural features of the Al-6Mg₂Si alloy under different conditions, as shown in **Fig. 5** and **Fig. 6**). The eutectic cellular structures were observed in the L-PBFed samples with the mean size of $\sim 1 \mu\text{m}$, which was composed of α -Al and Mg₂Si phases (**Fig. 5a**). For the DA-150 and DA-180 samples, the morphology and size of cellular structures were essentially unchanged (**Figs. 5b&c**). It is noteworthy that the cellular structures were partially disrupted and enlarged because of the precipitation and coarsening of Mg₂Si particles after DA-210 treatment (**Fig. 5d**). Within the AT-300 samples, the cellular structures were completely disrupted in the α -Al matrix. Meanwhile the size of uniformly distributed Mg₂Si particles within α -Al matrix is $\sim 256 \text{ nm}$ (based on the Image J Pro Plus software calculated) (**Fig. 5e**). Moreover, the size of coarsened Mg₂Si particles increased to $1.38 \mu\text{m}$ in the SAT-490/150 samples (**Fig. 5f**). In addition, the composition of coarsened particles within SAT-490/150 sample was determined via SEM-EDS in **Fig. 6**. The coarsened particles were mainly consisting of Mg/Si element, which confirms the formation of Mg₂Si particles.

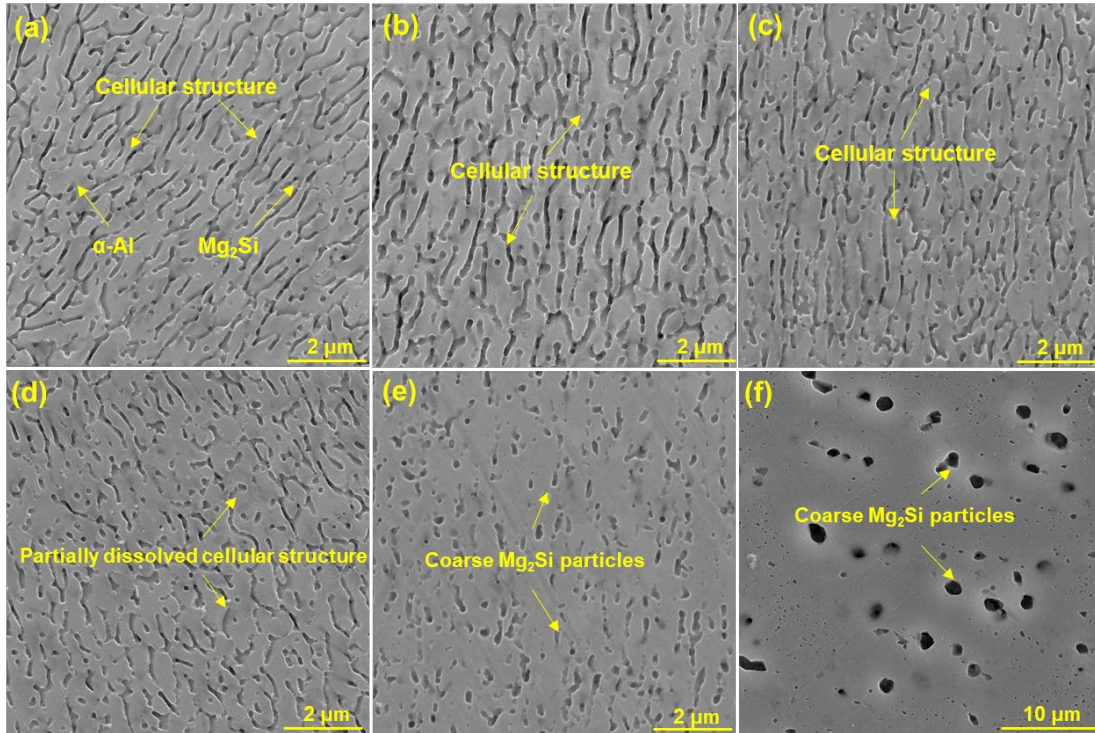


Fig. 5. SEM micrographs displaying the typical microstructures of the Al-6Mg₂Si alloy: (a) L-PBFed, (b) DA-150, (c) DA-180, (d) DA-210, (e) AT-300 and (f) SAT-490/150. Note the region characterized by SEM is located in the melt pool centre.

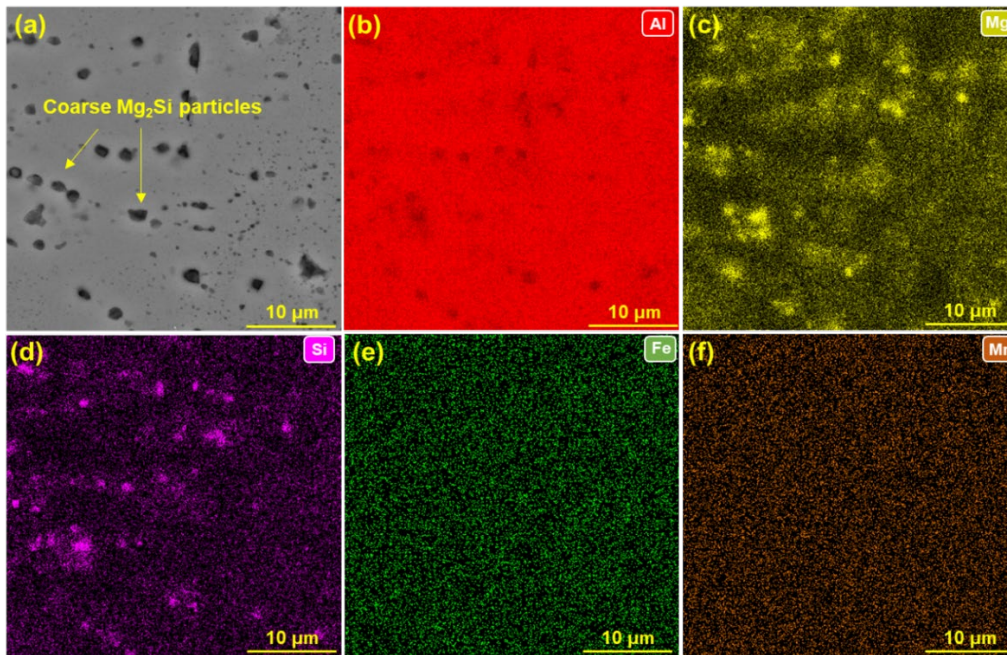


Fig. 6. SEM-EDS images revealing the coarsened particles of the SAT-490/150 sample including the Al, Mg, Si, Fe and Mn element.

Fig. 7 shows the EBSD-inverse pole figures (IPFs) of the Al-6Mg₂Si alloy along building direction under different conditions. The α -Al grain was composed of the columnar and equiaxed grain in L-PBFed state (**Fig. 7a**), which was closely associated with the high G and R during L-PBF process. The columnar grains also tended to grow

epitaxially along the building direction. The aspect ratios of α -Al grains in different samples are shown in **Fig. 8**. It is seen that the aspect ratios were not significantly changed between the L-PBFed condition and DA-treated condition. In comparison, the grains with the aspect ratio of below 2 decreased to 21.2 % of AT-300 samples and 19.3 % of SAT-490/150 samples, and the grains with the aspect ratio of above 4 increased to 26.5 % and 25.6 %, respectively. This confirmed that both the size and the fraction of columnar grains increased after AT-300 and SAT-490/150 treatments.

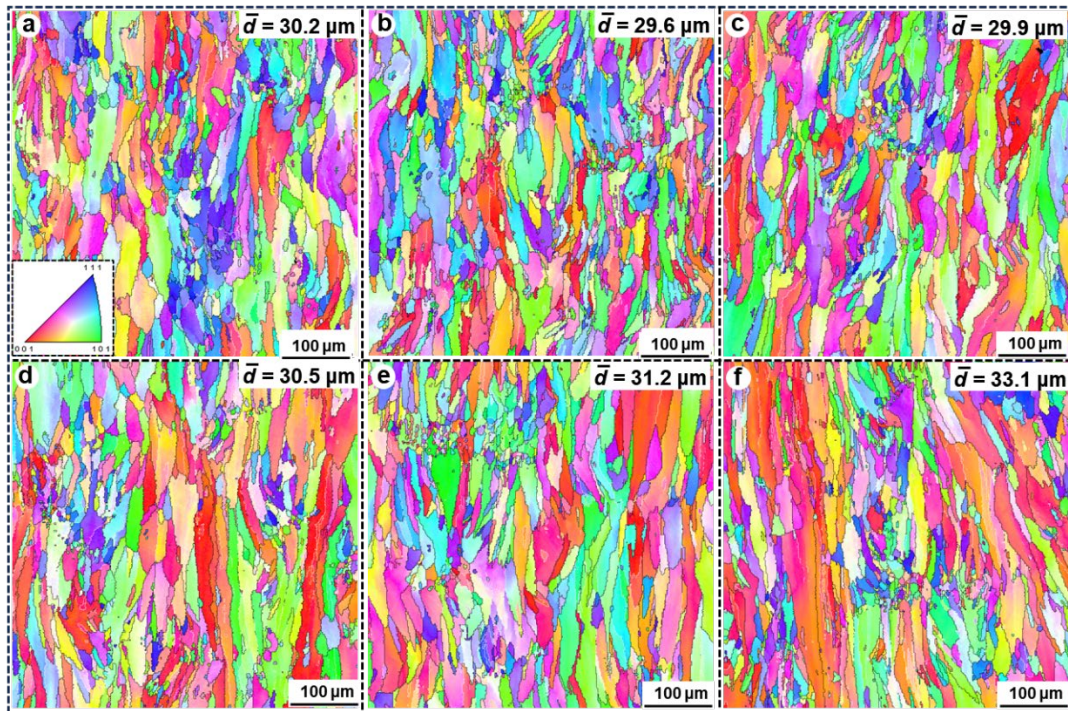


Fig. 7 EBSD-IPF maps showing the Al-6Mg₂Si alloy along the building direction under different conditions: (a) L-PBFed, (b) DA-150, (c) DA-180, (d) DA-210, (e) AT-300, (f) SAT-490/150.

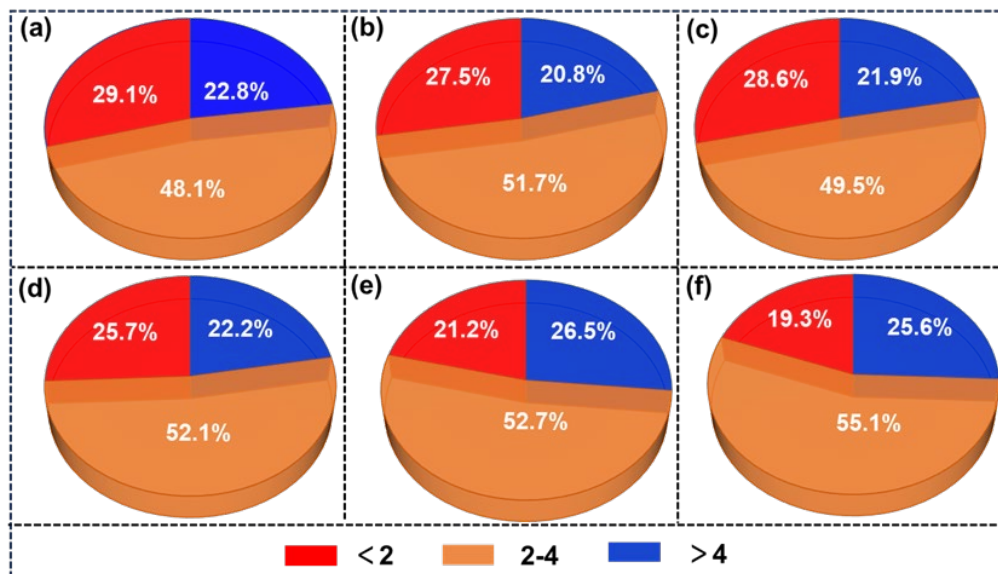


Fig. 8 The aspect ratio of the Al-6Mg₂Si alloy under different conditions along the building direction:

(a) L-PBFed, (b) DA-150, (c) DA-180, (d) DA-210, (e) AT-300, (f) SAT-490/150.

TEM was further employed to examine the microstructural evolution of L-PBFed Al-6Mg₂Si alloy, in which a superior strength enhancement was achieved (Figs. 9-10). The typical cellular structure was homogeneously distributed, as shown in Fig. 9a. Correspondingly, the high angle annular dark field-scanning TEM (HAADF-TEM) and the element distribution mapping showed that Mg/Si element were primarily present at the cellular structure boundaries, which confirms the formation of eutectic Mg₂Si. In addition, the orientation relationship (OR) between α -Al and Mg₂Si was detected using high-resolution TEM (HR-TEM) (Figs. 9c&d). The Al/Mg₂Si interface exhibited a coherent OR with $(11\bar{1})_{\alpha\text{-Al}}//(\bar{2}\bar{2}0)_{\text{Mg}_2\text{Si}}$, $[011]_{\alpha\text{-Al}}//[\bar{1}12]_{\text{Mg}_2\text{Si}}$. Correspondingly, the interplanar spacing of α -Al matrix was 0.1457 nm for $(02\bar{2})_{\text{Al}}$ plane and Mg₂Si phase was 0.3692 nm for $(1\bar{1}1)_{\text{Mg}_2\text{Si}}$ plane via and fast Fourier transforms (FFT). The interaction between Mg₂Si particles and dislocations also provided a strong basis for strengthening (Figs. 9e&f).

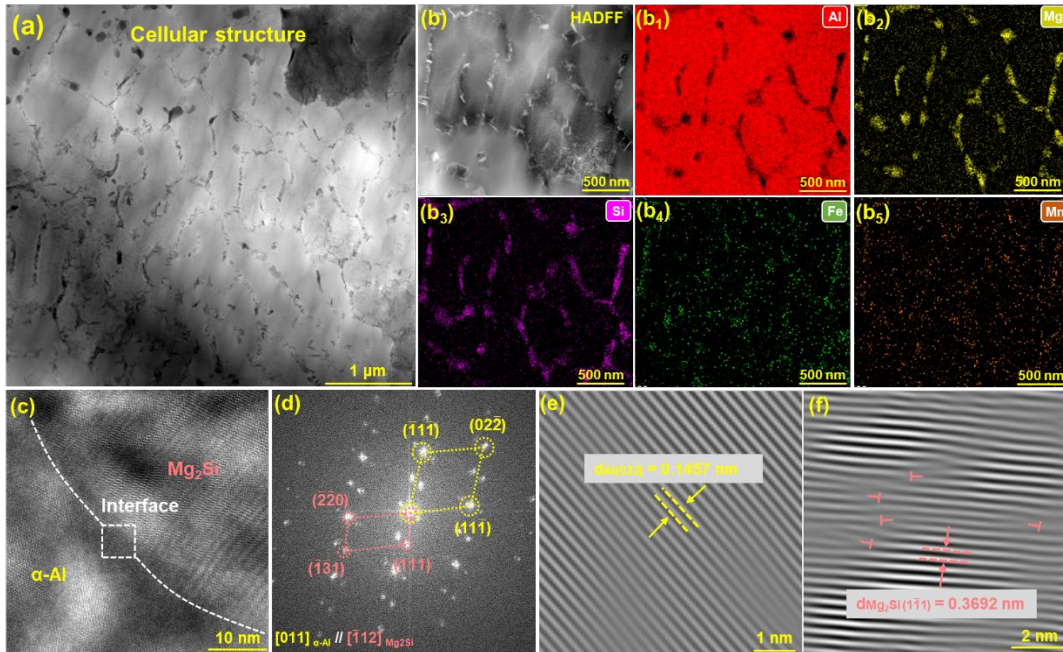


Fig. 9 TEM images displaying the typical microstructural features of the L-PBFed Al-6Mg₂Si alloy: (a) the eutectic cellular structure; (b, b₁-b₅) HAADF-STEM micrographs of cellular structure, and EDS mapping of Al, Mg, Si, Fe, and Mn element; (c) the α -Al/Mg₂Si interface; (d) FFT pattern of α -Al/Mg₂Si interface along $[011]_{\alpha\text{-Al}}//[\bar{1}12]_{\text{Mg}_2\text{Si}}$; (e) IFFT pattern of part along $(02\bar{2})_{\alpha\text{-Al}}$ and (f) IFFT pattern of part along $(1\bar{1}1)_{\text{Mg}_2\text{Si}}$. Note: the region characterized by TEM is located at the melt pool centre.

Fig. 10 displays the detailed microstructural characteristics of the DA-150 samples. It is seen that no distinguished differences were observed between the DA-150 and the L-PBFed samples in terms of the cellular structures and Mg₂Si eutectics, as shown in **Fig. 10a**. Meanwhile, the interaction between eutectic Mg₂Si phase and dislocations as

well as fine precipitates was also detected in **Fig. 10b**, and the high-magnification TEM image in **Fig. 10c** indicated that these precipitates primarily exhibited spherical and lath-shaped morphologies. Combined with the results of HAADF-STEM images and FFT pattern (**Figs. 10d&h**), these precipitates with enriched Mg/Si elements were identified as the metastable β'' phases (Mg_5Si_6 , C-centred monoclinic, $a = 1.516 \text{ nm}$, $b = 0.405 \text{ nm}$, $c = 0.674 \text{ nm}$ and $\beta = 105.3^\circ$ [29]), which was the main contributor to improved strength of the as-aged Al-Mg-Si alloy [30].

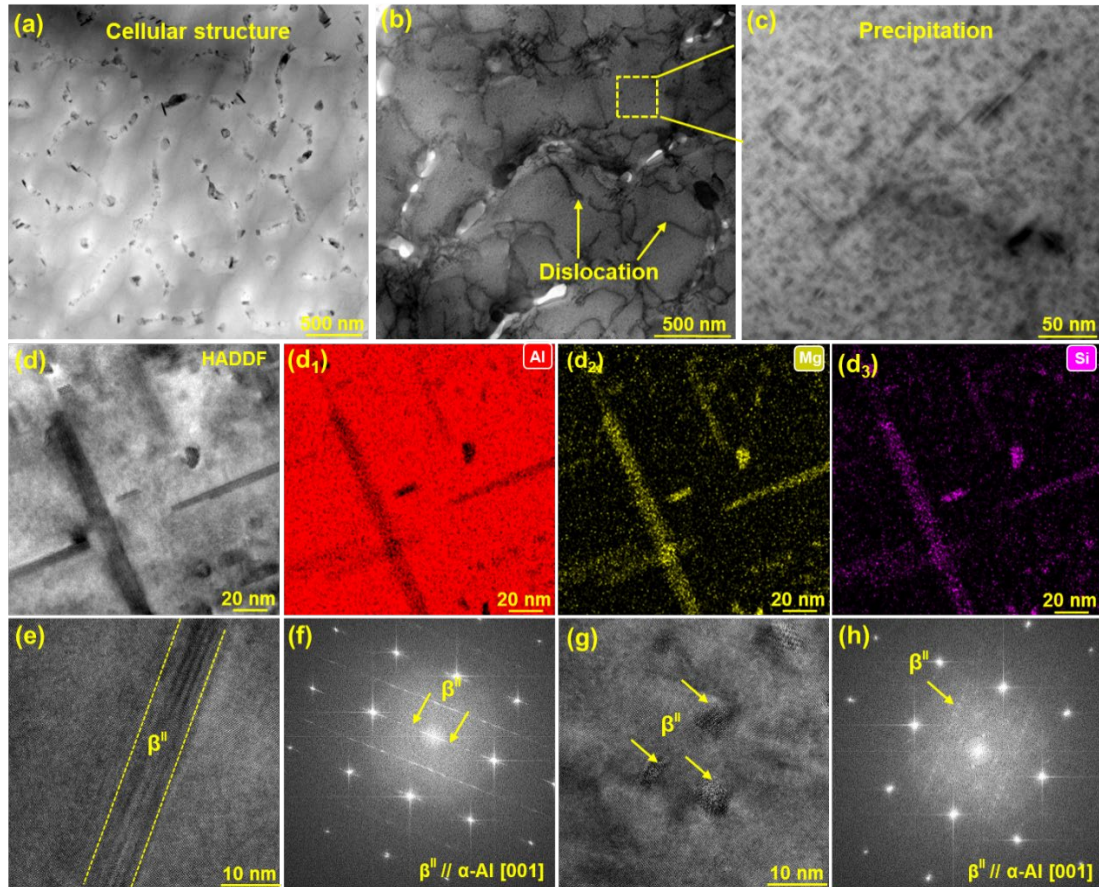


Fig. 10 TEM images of the microstructural characterization of the DA-150 samples: (a) BF-TEM micrographs of the eutectic Mg_2Si cellular structure; (b) a large number of precipitation with dislocation in cellular structure; (c) the precipitation distribution at the cellular structure interior (d, d₁-d₃) HAADF-STEM micrographs of β'' and EDS mapping of Al, Mg, and Si element; (e, f) HR-TEM of lath-shaped β'' precipitation and FFT pattern; (g, h) HR-TEM of spherical β'' precipitation and FFT pattern.

4. Discussion

4.1 The effect of heat treatment on microstructural evolution

The variations in mechanical properties of the L-PBFed Al-6Mg₂Si alloy during different annealing treatment is mainly ascribed to the microstructural evolution, particularly for the cellular structures and precipitates. **Fig. 11** illustrates the schematic

diagrams of microstructural features under different conditions. The L-PBF process can offer the rapid solidification with large temperature gradients ($> 10^5$ °C/m) and high cooling rates ($10^5 \sim 10^6$ °C/s) characteristics, which form unique non-equilibrium microstructure [31]. The central of melt pool of Al-6Mg₂Si alloy are mainly composed of the Al/Mg₂Si cellular structure, which are formed as a product of eutectic reaction in the final stage of solidification [32, 33]. Moreover, the non-equilibrium solidification can promote the solid solution of Mg and Si element into the α -Al matrix. This offers a thermodynamic source of nucleation, facilitating the formation of precipitates and lowering the energy barrier required for nucleation in subsequent direct ageing treatment [34, 35]. Currently, the sequence of precipitation in Al-Mg-Si alloy is: SSS (supersaturated solid solution) \rightarrow Mg/Si solute clusters \rightarrow GP zones \rightarrow β'' (Mg₅Si₆ or Mg₅Al₂Si₄) \rightarrow β' (Al₃Mg₉Si₇) \rightarrow β [36]. Under the DA-150 condition, the microstructure is mainly featured by the remained cellular structures, the spherical and lath-shaped β'' distributed within the interior of cellular structures (**Fig. 11b**), in which β'' phase is widely regarded as important contributor for strength enhancement in cast Al-Mg-Si alloy [37, 38]. It is also worth noting that the characteristics of cellular structure (e.g., size and morphology) are changed considerably after AT condition. The Al/Mg₂Si cellular structures are completely broken up and transformed into Mg₂Si particles. The metastable β'' phases further grow up and transform to stable Mg₂Si particles under the AT-300 condition (**Fig. 11c**), the larger and irregular coarsened Mg₂Si particles are further detected under SAT-490/150 condition (**Fig. 11d**). Overall, it is clear that the Al/Mg₂Si cellular structure and β'' phase are metastable, and gradually evolve into more stable microstructure during the AT and SAT condition. Based on the Ostwald ripening mechanism [39], the volume fraction of Mg₂Si particles increases with increasing the annealing temperatures and/or times, in consistent with a corresponding increase in the average size. Therefore, the metastable Al/Mg₂Si cellular structures and β'' phases of L-PBFed Al-6Mg₂Si alloys are gradually transformed into a more stable microstructure during the following AT and SAT conditions.

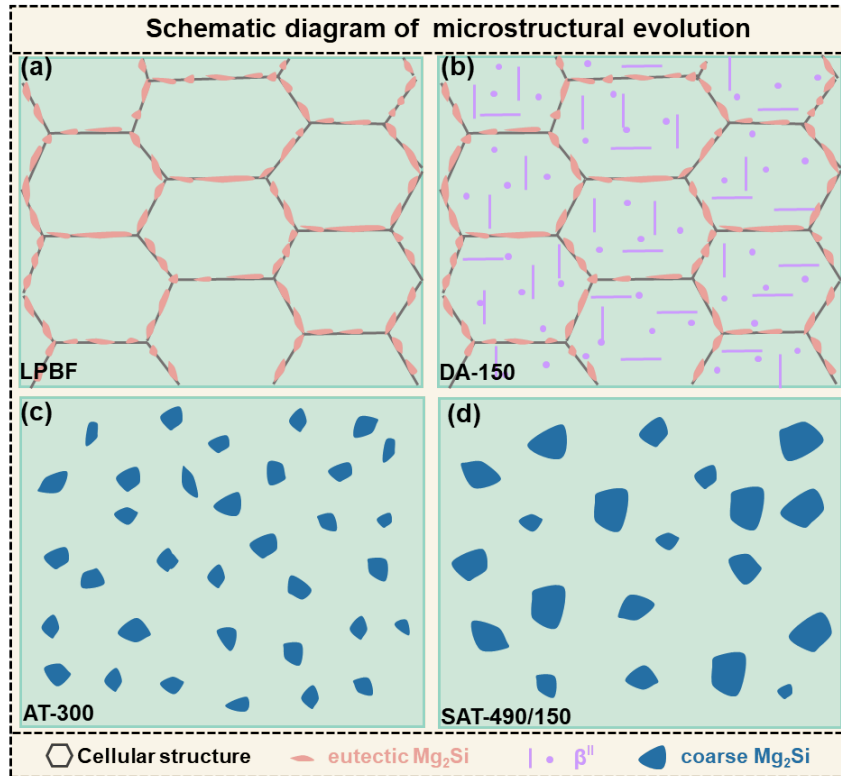


Fig. 11 Schematic diagram showing microstructural evolution under different treatments: (a) L-PBFed, (b) DA-150, (c) AT-300, (d) SAT-490/150.

4.2 The effect of heat treatment on the mechanical properties with related strengthening mechanisms

The excellent mechanical properties are ascribed to the unique hierarchical microstructure in the L-PBFed Al-6Mg₂Si alloy compared with the conventional Al-Mg-Si alloys [40, 41], which improve via subsequent ageing treatment further. A representative diagram showing the interaction between the hierarchical microstructure and dislocations is illustrated in **Fig. 12**, in which the interactions between dislocations and fine α -Al grains, sub-micrometre-sized Al/Mg₂Si eutectics and nanosized precipitates and solutes were detected in the DA-150 samples. The excellent mechanical properties are primarily attributed to the following aspects: (i) the fine α -Al grains ($\sim 30 \mu\text{m}$) lead to an effective grain boundary strengthening; (ii) the fine Al/Mg₂Si cellular structure play a key role in potentiating the pinning force of dislocation movement, and the dislocations entrapped within and at the sub-boundaries of Mg₂Si eutectics induce a strength improvement; (iii) the solid solubility of Mg/Si element is considerably increased because of the extremely high cooling rate of L-PBF process, which induces an enhancement in solid solution strengthening; (iv) the ultrafine β'' precipitates (5-30 nm) offer effective precipitation strengthening; (v) the strength enhancement contribution also comes from the pre-existence of a high-density

dislocations, which attributed to form the high strain induced via rapid solidification and the thermal contraction stresses. However, the hierarchical microstructure is destroyed under the AT-300 and SAT-490/150 conditions, and corresponding the strength is greatly reduced. The potential causes can be ascribed to the following: (i) the breakdown of Al/Mg₂Si eutectics reduces the cellular boundary strengthening; (ii) the reduction of the Mg and Si contents and (iii) the transformation of fine β'' precipitates into coarse Mg₂Si phase; (iv) the decrease in dislocation density after annealing treatment at high temperatures.

To get insights between the evolution of non-equilibrium microstructures and mechanical properties during different heat treatments further, the potential strengthening mechanisms are quantitatively assessed. The strengthening mechanisms consist of grain boundary strengthening (σ_{gb}), cellular boundary strengthening (σ_{cb}), solid solution strengthening (σ_{ss}), dislocation strengthening (σ_{dis}) and precipitation strengthening (σ_p). **Fig. 12** presents a comparison of the calculated and experimentally measured contributions to the YS. Obviously, the Al/Mg₂Si cellular structures with dislocation play an important role in strengthening of the L-PBFed Al-6Mg₂Si alloy. Meanwhile, the high-level solutes and fine α-Al grains offer high σ_{ss} and σ_{gb} , resulting in a comparative σ_{YS} of 338 MPa. In the DA-150 sample, the σ_{cb} , σ_{dis} and σ_{gb} still vary within a small range. The formation of nano-sized β'' particles significantly improve the contribution of σ_p (108 MPa) and weaken the effect of σ_{ss} due to the transformation from solutes to nano-sized precipitates. Correspondingly, the σ_{YS} increases by 20 % in comparison with that in the as-LPBFed state, achieving an excellent yield strength (407 MPa). However, the absence of σ_{cb} is ascribed to the complete breakdown of cellular structures in the AT-300 samples. The broken cellular structures, the fine nano-sized β'' particles as well as the residual solutes are transformed into the coarsened Mg₂Si phases, leading to a decreased yield strength of (187 MPa). Under the SAT-490/150 condition, the coarsened Mg₂Si phases with a low fraction induces only 11 MPa of σ_p and extremely low yield strength of 135 MPa. It is also necessary to consider the load-bearing strengthening ($\Delta\sigma_{Load}$) induced via the continuous cellular network [42, 43]. It is expected that the Al/Mg₂Si cellular network can withstand high stresses through the interphase load transfer effect under loading in the L-PBF and DA-150 samples. In contrast, the Al/Mg₂Si cellular structure was broken in AT-300 and SAT-490/150 samples, the effect of load-bearing strengthening was then reduced, which is partially accountable for the reduction in YS. The detailed calculation data is provided in the supplementary material.

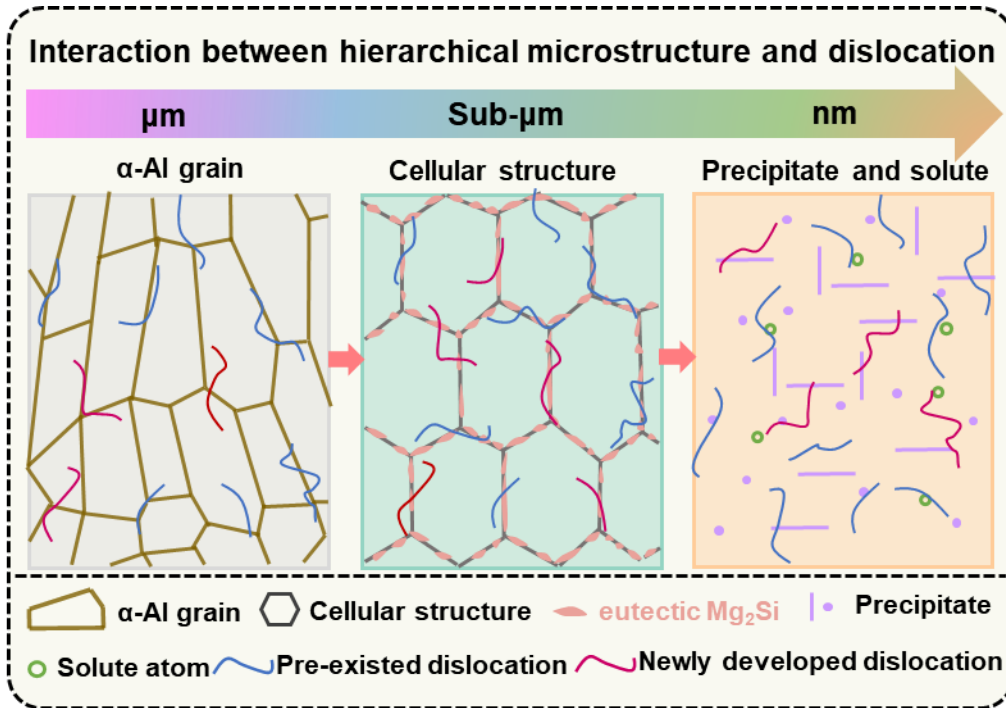


Fig. 12. Schematic diagram of the interaction between hierarchical microstructure and dislocations.

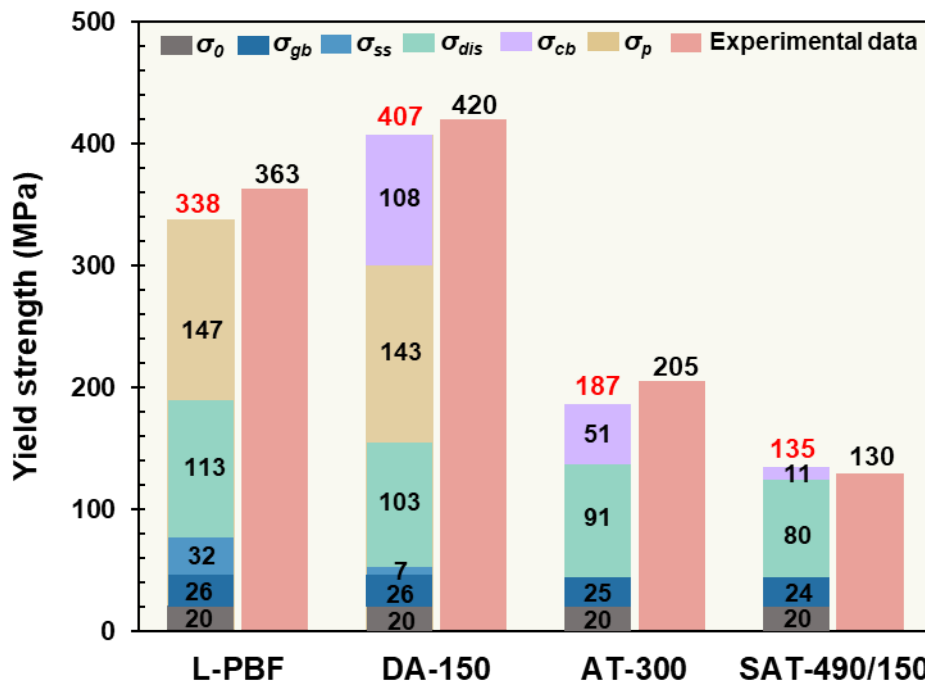


Fig. 13. The comparison of calculated and experimentally measured contributions to YS of Al-6Mg₂Si alloy under different conditions.

5. Conclusions

This study demonstrates the effects of different heat treatment on the microstructural evolution and mechanical response of L-PBFed Al-6Mg₂Si alloy. The corresponding conclusions can be summarized as follow:

- (1) The L-PBFed sample is mainly strengthened by the interaction between dislocations and Al/Mg₂Si cellular structures within fine α -Al grains formed during the rapid solidification characteristics of L-PBF, with YS of 363 MPa, UTS of 436 MPa and El of 9.3 %.
- (2) The typical melt pool structures and cellular structures were not significantly changed under as-aged condition. The DA-150 samples (aged at 150 °C for 8 h) exhibited a superior combination of strength-ductility synergy, in which YS, UTS and El were 420 MPa, 496 MPa and 9.5 %, respectively. The enhance in strength was mainly responsible for the formation of nano-size β'' precipitates.
- (3) The Al/Mg₂Si eutectics were totally disrupted and transformed into coarse Mg₂Si particles under the as-annealed conditions. The AT-300 sample exhibited a decreased YS of 205 MPa and increased El of 10.7%. Both the YS and UTS of the SAT-490/150 samples were decreased further due to the totally broken Mg₂Si eutectics, the coarsened Mg₂Si phase and the reduced density of dislocations.
- (4) Direct ageing is demonstrated as an effective heat treatment method for improving the strengthening of L-PBFed Al-6Mg₂Si alloy, which provides a reference for optimizing the heat treatment process of other L-PBFed Al alloys.

Credit authorship contribution statement

Tao Wen: Experiments, data collection and analysis, writing - original draft.
Jiaying Wang: Experiments and data collection, writing – review & editing, results review.
Feipeng Yang: Experiments and data analysis.
Mengzhen Zhu: Conceptualization and investigation.
Yimou Luo: Conceptualization and investigation.
Zhilin Liu: Conceptualization, writing – review & editing, supervision.
Xixi Dong: Conceptualization, writing – review & editing, supervision.
Hailin Yang: Conceptualization, funding acquisition, project management, supervision, writing - editing & review.
Shouxun Ji: Conceptualization, writing - editing & review.

Declaration of Competing Interest

The authors declare that they have no known competing financial interests or personal relationships that could have appeared to influence the work reported in this paper.

Data availability

Data will be made available on request.

Acknowledgement

Financial support from National Natural Science Foundation of China (Grant No. 52071343) and Leading Innovation and Entrepreneurship Team of Zhejiang Province – Automotive Light Alloy Innovation Team (2022R01018) are gratefully acknowledged.

Reference:

- [1] J.Y. Wang, J.B. Gao, H.L. Yang, F.P. Yang, T. Wen, Z.L. Liu, L.J. Zhang, S.X. Ji, High-strength Al-5Mg2Si-2Mg-2Fe alloy with extremely high Fe content for green industrial application through additive manufacturing, *Virtual. Phys. Prototy.* 18 (2023) 2235587.
- [2] F.P. Yang, T. Wen, L. Zhang, J.Y. Wang, S.L. Huang, S.X. Ji, H.L. Yang, Role of inclination angle on columnar-to-equiaxed transition in the eutectic Al-5Mg-2Si alloy fabricated by laser powder bed fusion, *J Chet. South Univ.* 2024, 31(8).
- [3] D. Herzog, V. Seyda, E. Wycisk, C. Emmelmann, Additive manufacturing of metals, *Acta Mater.* 117 (2016) 371–392.
- [4] A. Prasad, L. Yuan, P. Lee, M. Patel, D. Qiu, M. Easton, D. StJohn, Towards understanding grain nucleation under Additive Manufacturing solidification conditions, *Acta Mater.* 195 (2020) 392–403.
- [5] J.H. Martin, B.D. Yahata, J.M. Hundley, J.A. Mayer, T.A. Schaedler, T.M. Pollock, 3D printing of high-strength aluminium alloys, *Nature* 549 (2017) 365-369.
- [6] Q.Y. Tan, J.Q. Zhang, Q. Sun, Z.Q. Fan, G. Li, Y. Yin, Y.G. Liu, M.X. Zhang, Inoculation treatment of an additively manufactured 2024 aluminium alloy with titanium nanoparticles, *Acta Mater.* 196 (2020) 1-16.
- [7] G. Li, Y.H. Huang, X.W. Li, C. Guo, Q. Zhu, J. Lu, Laser powder bed fusion of nano-titania modified 2219 aluminium alloy with superior mechanical properties at both room and elevated temperatures: The significant impact of solute, *Addit. Manuf.* 60 (2022) 103296.
- [8] G.C. Li, B. Tunca, S. Senol, M. Casata, Y. Wu, Z. Chen, K. Vanmeensel, Revealing the precipitation behavior of crack-free TiB₂/Al-Zn-Mg-Cu composites manufactured by Laser Powder Bed Fusion, *Addit. Manuf.* 66 (2023) 103460.
- [9] J. Suryawanshi, K.G. Prashanth, S. Scudino, J. Eckert, O. Prakash, U. Ramamurty, Simultaneous enhancements of strength and toughness in an Al-12Si alloy synthesized using selective laser melting, *Acta Mater.* 115 (2016) 285-294.

- [10] L. Thijs, K. Kempen, J.P. Kruth, J.V. Humbeeck, Fine-structured aluminium products with controllable texture by selective laser melting of pre-alloyed AlSi10Mg powder, *Acta Mater.* 61 (2013) 1809-1819.
- [11] R. Ma, C. Peng, Z. Cai, R. Wang, Z. Zhou, X. Li, X. Cao, Effect of bimodal microstructure on the tensile properties of selective laser melt Al-Mg-Sc-Zr alloy, *J. Alloys Compd.* 815 (2020) 152422.
- [12] Y. Shi, K. Yang, S.K. Kairy, F. Palm, X. Wu, P.A. Rometsch, Effect of platform temperature on the porosity, microstructure and mechanical properties of an Al-Mg-Sc-Zr alloy fabricated by selective laser melting, *Mater. Sci. Eng. A* 732 (2018) 41–52.
- [13] X. Xiao, Y. Guo, R. Zhang, D. Bayoumy, H. Shen, J. Li, K. Gan, K. Zhang, Y. Zhu, A. Huang, Achieving uniform plasticity in a high strength Al-Mn-Sc based alloy through laser-directed energy deposition, *Addit. Manuf.* 60 (2022) 103273.
- [14] A. Mehta, L. Zhou, T. Huynh, S. Park, H. Hyer, S.T. Song, Y.L. Bai, D.D. Imholte, N.E. Woolstenhulme, D.M. Wachs, Y.H. Sohn, Additive manufacturing and mechanical properties of the dense and crack free Zr-modified aluminium alloy 6061 fabricated by the laser powder bed fusion, *Addit. Manuf.* 41 (2021) 101966.
- [15] Z. Zhang, D. Li, S. Li, H. Deng, S. Zhang, J. Fang, H. Yuan, B. Deng, L. Qi, Effect of direct aging treatment on microstructure, mechanical and corrosion properties of a Si-Zr-Er modified Al-Zn-Mg-Cu alloy prepared by selective laser melting technology, *Mater. Char.* 194 (2022) 112459.
- [16] Q.Z. Wang, N. Kang, X. Lin, M. EL Mansori, Y. Liu, J.L. Lu a,c, Y.F. Wang,H.Z. Chai, W.D. Huang, On the Si-induced microstructure evolution, solidification cracking healing and strengthening behavior of laser powder bed fusion additive manufactured Al-Cu-Mg/Si alloys, *J Mater. Process. Tech.* 313 (2023) 117860.
- [17] H.W. Zhu, J.W. Sun, Y.J. Guo, X.X. Xu, Y.C. Huang, Z.D. Jiang, G.H. Wu, J.F. Li, W.C. Liu, Effects of post heat treatment on the microstructure and mechanical properties of selective laser melted AlSi10Mg alloys, *Mater. Sci. Eng. A* 894 (2024) 146195.
- [18] L. Zhou, H. Pan, H. Hyer, S. Park, Y.L. Bai, B. McWilliams, K. Cho, Y. Sohn, Microstructure and tensile property of a novel AlZnMgScZr alloy additively manufactured by gas atomization and laser powder bed fusion, *Scripta Mater.* 158 (2019) 24-28.
- [19] N. Takata, H. Kodaira, K. Sekizawa, A. Suzuki, M. Kobashi, Change in microstructure of selectively laser melted AlSi10Mg alloy with heat treatments, *Mater. Sci. Eng. A* 704 (2017) 218–228.

- [20] J. Fiocchi, C.A. Biffi, C. Colombo, L.M. Vergani, A. Tuissi, Ad Hoc heat treatments for selective laser melted AlSi10Mg alloy aimed at stress-relieving and enhancing mechanical performances, *JOM* 72 (2020) 1118–1127.
- [21] S. Chen, Q. Tan, W. Gao, G. Wu, J. Fan, Z. Feng, T. Huang, A.W. Godfrey, M. Zhang, X. Huang, Effect of heat treatment on the anisotropy in mechanical properties of selective laser melted AlSi10Mg, *Mater. Sci. Eng., A* 858 (2022) 144130.
- [22] C.G. Wang, J.X. Zhu, G.W. Wang, Y. Qin, M.Y. Sun, J.L. Yang, X.F. Shen, S. K. Huang, Effect of building orientation and heat treatment on the anisotropic tensile properties of AlSi10Mg fabricated by selective laser melting, *J. Alloys Compd.* 895 (2022) 162665.
- [23] T.H. Park, M.S. Baek, H. Hyer, Y.H. Sohn, K.A. Lee, Effect of direct ageing on the microstructure and tensile properties of AlSi10Mg alloy manufactured by selective laser melting process, *Mater. Charact.* 176 (2021) 111113.
- [24] R.D. Li, M.B. Wang, Z.M. Li, P. Cao, T.C. Yuan, H.B. Zhu, Developing a high-strength Al-Mg-Si-Sc-Zr alloy for selective laser melting: crack-inhibiting and multiple strengthening mechanisms, *Acta Mater.* 193 (2020) 83–98.
- [25] H.L. Yang, Y.Y. Zhang, J.Y. Wang, Z.L. Liu, C.H. Liu, S.X. Ji, Additive manufacturing of a high strength Al-5Mg₂Si-2Mg alloy: Microstructure and mechanical properties, *J. Mater. Sci. Tech.* 91 (2021) 215-223.
- [26] F.P. Yang, J.Y. Wang, T. Wen, S.L. Huang, L. Zhou, H.L. Yang, S.X. Ji, Manipulating microstructure and mechanical properties of laser powder bed fusion processed hypo-eutectic Al-13.3Mg₂Si alloy via annealing, *J. Alloys. Compd.* 967 (2023) 171805.
- [27] T. Wen, J.Y. Wang, Z.C. Li, F.P. Yang, Z.L. Liu, H.L. Yang, S.X. Ji, Microstructural evolution and strengthening mechanisms of a high-strength Al-Mg-Si alloy processed by laser powder bed fusion and ageing treatment, *Mater. Charact.* 209 (2024) 113754.
- [28] T. Wen, Z.C. Li, J.Y. Wang, Y.M. Luo, F.P. Yang, Z.L. Liu, D. Qiu, H.L. Yang, S.X. Ji, From crack-prone to crack-free: eliminating cracks in additive manufacturing of high-strength Mg₂Si-modified Al-Mg-Si alloys, *J. Mater. Sci. Tech.* 204 (2025) 276-291.
- [29] S.J. Andersen, H.W. Zandbergen, J. Jansen, C. Træholt, U. Tundal, O. Reiso, The crystal structure of the β'' phase in Al–Mg–Si alloys, *Acta Mater.* 46 (1998) 3283–3298.
- [30] M.J. Yang, A. Orekhov, Z.Y. Hu, M. Feng, S.B. Jin, G. Sha, K. Li, V. Samaee, M. Song, Y. Du, G.V. Tendeloo, D. Schryvers, Shearing and rotation of β'' and β' precipitates in an Al-Mg-Si alloy under tensile deformation: In-situ and ex-situ studies,

Acta Mater. 220 (2021), 117310.

[31] A. Prasad, L. Yuan, P. Lee, M. Patel, D. Qiu, M. Easton, D. StJohn, Towards understanding grain nucleation under Additive Manufacturing solidification conditions, Acta Mater. 195 (2020) 392–403.

[32] J. Wu, X.Q. Wang, W. Wang, M.M. Attallah, M.H. Loretto, Microstructure and strength of selectively laser melted AlSi10Mg, Acta Mater. 117 (2016) 311–320.

[33] K.G. Prashanth, J. Eckert, Formation of metastable cellular microstructures in selective laser melted alloys, J. Alloy. Compd. 707 (2017) 27–34.

[34] Q. Luo, Y.L. Guo, B. Liu, Y.J. Feng, J.Y. Zhang, Q. Li, K.C. Chou, Thermodynamics and kinetics of phase transformation in rare earth–magnesium alloys: A critical review. J. Mater. Sci. Tech. 44 (2020) 171-190.

[35] Q. Luo, J.D. Li, B. Li, B. Liu, H.Y. Shao, Q. Li, Kinetics in Mg-based hydrogen storage materials: Enhancement and mechanism, J. Magnes. Alloy. 7 (2019) 58-71.

[36] J. Fiocchi, A. Tusissi, C.A. Biffi. Heat treatment of aluminium alloys produced by laser powder bed fusion: A review, Mater. Des. 204 (2021) 109651.

[37] G.A. Edwards, K. Stiller, G.L. Dunlop, M.J. Couper, The precipitation sequence in Al–Mg–Si alloys, Acta Mater. 46 (1998) 3893–3904.

[38] Q. Cai, C.L. Mendis, I.T.H. Chang, Z. Fan, Effect of short T6 heat treatment on the microstructure and the mechanical properties of newly developed die-cast Al–Si–Mg–Mn alloys, Mater. Sci. Eng., A 788 (2020), 139610.

[39] C. Gao, Z. Liu, Z. Xiao, W. Zhang, K. Wong, A.H. Akbarzadeh, Effect of heat treatment on SLM-fabricated TiN/AlSi10Mg composites: Microstructural evolution and mechanical properties, J. Alloy. Compd. 853 (2021) 156722.

[40] S. Ji, F. Yan, Z. Fan, Development of a high strength Al-Mg₂Si-Mg-Zn based alloy for high pressure die casting, Mater. Sci. Eng., A. 626 (2015) 165-174.

[41] X. Zhu, H. Yang, X. Dong, S. Ji, The effects of varying Mg and Si levels on the microstructural inhomogeneity and eutectic Mg₂Si morphology in die-cast Al-Mg-Si alloys, J. Mater. Sci. 54 (2019) 5773-5787.

[42] X.X. Zhang, A. Lutz, H. Andra, M. Lahres, W.M. Gan, E. Maawad, C. Emmelmann, Evolution of microscopic strains, stresses, and dislocation density during in-situ tensile loading of additively manufactured AlSi10Mg alloy, Int. J. Plast. 139 (2021) 102946.

[43] X.X. Zhang, A. Lutz, H. Andra, M. Lahres, D. Sittig, E. Maawad, W.M. Gan, D. Knoop, An additively manufactured and direct-aged AlSi_{3.5}Mg_{2.5} alloy with superior strength and ductility: micromechanical mechanisms, Int. J. Plast. 146 (2021) 103083.